COMMUNICATION

Check for updates

Impacts of pore size in binding dynamics of per- and polyfluoroalkyl substances (PFAS) on modified graphene materials

Timothy C. Schutt, [ID] *[a] Caitlin G. Bresnahan, [ID] [a] Timothy C. Ricard [ID] [b] and Manoj K. Shukla*[a]

Per- and polyfluoroalkyl substances (PFAS) have become ubiquitous surfactants in the environment with long lifetimes, and emerging toxic effects. Capture and removal of PFAS from aqueous media is an important step in the treatment train along with the concentration and destruction of PFAS. Particularly PFAS with shorter alkyl chain lengths have proven to be difficult to remove from water. As a result of partial degradation from longer PFAS's as well as their enhanced mobility in the environment, short-chain PFAS are very prolific making them a high-target focus for PFAS removal research. Using molecular dynamics simulations of functionalized graphene oxide pores, we have shown that the selectivity and capacity of adsorption media for differing tail lengths of linear PFAS are impacted by the size of the material's nanoporosity. The relationship between PFAS transport and pore size is not monotonic and different PFAS have different critical pore diameters with a minimum in transport resistance enabling an effective mechanism for PFAS specificity. More pragmatically, we have identified critical pore diameters that impact the thermodynamics and kinetics of PFAS binding and transport. For example, selectivity towards PFBA is highest in pores of 9 Å diameter. These results imply design parameters with which to tune adsorption media to different partitioning, transport, and selectivity towards different PFAS.

Environmental significance

The findings in this manuscript enable design and adsorption specificity towards priority per- and polyfluoroalkyl substance (PFAS) pollutants and especially short-chain versions. Short-chain PFAS are important contaminants to be able to remove due to their relatively high solubility in water systems, difficulty of removal, and toxicity impacts. Most adsorbents adsorb long chain PFAS more readily and at the expense of being able to adsorb short chain PFAS at capacity. PFAS molecules thread through nanopores at different rates based on their fluorinated tail length allowing for novel selectivity for specific PFAS species to adsorb more readily than others. Our results show that short chain PFAS can be preferentially transported and adsorbed over long chain PFAS in pore sizes of 8 to 10 Angstroms in diameter. In this concise manuscript we investigate the surprisingly non-monotonic response of PFAS transport as a function of pore size in graphene oxide and functionalized graphene oxide nanopores and discuss implications for adsorbent design principles.

Introduction

Per- and polyfluoroalkyl substances (PFAS) are a class of chemicals that have many useful attributes such as a hydrophilic head group, a hydrophobic tail group, the famously strong C–F bond, and they are oleophobic.[1] These properties make them ideal for use in manufacturing and industry including mining, aerospace, the semiconductor industry, the chemical industry, flame retardants and pharmaceuticals.[2]

Their anti-stick, anti-stain, and waterproof features make them an exemplary component of many household products including non-stick cookwares, cosmetics, cleaners, and much more.[3–5] The use of PFAS in so many spaces, and their longevity in the environment, has caused PFAS contamination to become a problem across most of the world.[6–14] Unfortunately, PFAS have been connected to a slew of health issues like cancers, heart issues, and developmental problems.[15–18] Thus, remediation techniques are desired.

PFAS are found in waterways across the globe.[2,6,9,10,14] Many PFAS remediation methods have been tested, and perform most efficiently on concentrated samples relative to the concentration of PFAS in the environment.[1,3,19] In order to use these methods efficiently, it is essential to uptake PFAS from dilute aqueous sources and up-concentrate the PFASs. Thus, highly selective adsorbent materials are necessary. Materials that have been used to remove PFAS from water include biochar,[20] functionalized graphene,[21] activated carbon,[22,23] and hydrogels,[24] though most do not perform as well for short chain PFAS capture as they do for long chain PFAS. Porous materials have shown promise for removing PFAS from the environment and can theoretically be tailored to have selectivity towards different

[a]US Army ERDC, Environmental Laboratory, 3909 Halls Ferry Rd, Vicksburg, Mississippi, 39180, USA. E-mail: timothy.c.schutt@erdc.dren.mil; manoj.k.shukla@erdc.dren.mil

[b]Oak Ridge Institute for Science and Education (ORISE), 1299 Bethel Valley Rd, Oak Ridge, Tennessee 37830, USA

© 2025 The Author(s). Published by the Royal Society of Chemistry

Environ. Sci.: Adv., 2025, **4**, 1587–1593 | 1587

types and sizes of PFAS.[25] Tighe *et al.*[26] have explored using high internal phase emulsion polymers, a porous sponge-like polymer, with the addition of quaternary amines and achieved a high adsorption capacity of 300 mg of PFOA per gram of polymer. Thompson *et al.*[27] modified a microfiltration membrane to see how functionalizing it with primary and quaternary amines impacts PFAS capture and found the membranes captured 90–99% of 100 ppb PFOA.

The pore-PFAS interactions of adsorption materials are of critical importance to their effectiveness. Metal organic frameworks (MOFs) and covalent organic frameworks (COFs) are porous materials that can be easily modified for a target molecule. Liu *et al.*[28] made MIL-101-Cr-QDMEN which showed an enhancement of adsorption capacity towards PFAS compared to the MOFs they studied. They found that the Cr^{3+} metal center acted as a PFOA adsorption cite. Yang *et al.*[29] compared MIL-100-Fe and MIL-101-Fe and found that both removed PFOA from water, but MIL-101-Fe performed better due to the pore structure and chemistry of the ligands. Sini *et al.*[30] found that UiO-67 performed better than UiO-66 at PFOA and PFOS capture. They believe the larger pore size played a role in the superior performance. Wang *et al.*[31] examined the influence of pore size by examining five COFs with diameter ranging from 1.2 to 4.1 nm. They found that the largest pore size performed poorly in comparison, and that the smallest pore size did not remove PFAS. They determined that a pore size that is 2.5–4 times the length of a PFAS is the best range for PFAS capture. Clearly the pore size and functionality of the pore is important for selective PFAS capture. In our work, we have explored how pore size, and functionality of the pore can impact the mechanism of specificity towards PFAS capture. In Wang *et al.*'s research,[31] nanobubbles were included in the simulation, which impacted how a PFAS approaches the COF.

Computational tools such as Molecular Dynamics (MD) and Density Functional Theory (DFT) enable the mechanistic explanation, prediction, and screening of PFAS adsorption. The adsorption mechanisms and effect of ionic surfaces such as clays have been characterized using surface partitioning and binding models in MD.[32,33] Graphene and modified graphene oxides have been shown to exhibit strong affinity for PFAS in water due to hydrophobic pockets formed at the aqueous interface.[34,35] Tuning the gap size between graphene oxide flakes through alkylation of the surface was shown to shift the selectivity to favor short-chain PFAS adsorption over long-chain PFAS.[36] And similarly, nanochannels with graphene oxide have targeted short chain PFAS adsorption through size exclusion and electrostatic effects.[37] Adsorption tunabilty *via* pore manipulation, surface modification, and the computationally screening of surfaces drives design of novel sorption media such as ultraporous silica nanoparticles.[38] Additional recent modeling advancements for PFAS removal include DFT and MD studies elucidating the reaction preferences of different PFAS structures for degradation by radicals,[39,40] and the design of deep eutectic solvents for liquid phase extraction.[41] In the current work, we considered neat water solution to tease out the direct effects of pore size and functionality on PFAS adsorption.

Methods

MD simulations were performed in the Amber MD package[42] with molecules parameterized by General Amber Force Field (GAFF)[43] for the bonds, angles, dihedrals, impropers, and van der Waals parameters. Charges were calculated by the RESP method[44] as implemented in antechamber[45] based on the underlying electronic structure as calculated at the MP2/cc-pVTZ level of theory/basis set in Gaussian16 *ab initio* package.[46] Charges calculated in this way have been demonstrated to reproduce dynamical data without a scaling factor required.[47] The graphene flakes were too large to calculate charges directly as whole structures. Instead, dibenzyl representations of each functionality were created and the change in charge of the carbons caused by the functional group being attached to the carbon, or attached to a neighboring carbon were transferred over to the larger flake carbons based on their proximity to given functional groups or edges. More information on that can be found in previous work by Bresnahan *et al.*[21] Explicit tip4pew water molecules[48] were used for the solvent phase.

All PFAS were tested against 4 functionalized flake types to observe the generalizability of trends *vs.* pore size and effect of pore wall chemistry. The 4 functionalization types are graphene oxide, fully fluorinated graphene, partially fluorinated graphene, and amide-functionalized graphene. The results of all 4 flake types are included in the SI. For clarity, the primary manuscript focuses on graphene oxide and fluorinated graphene as the most informative test cases. The degree of oxidation of the graphene is a significant factor in how the material will behave and how PFAS will adsorb to it or not. Past literature indicates that experimental graphene oxides tend to be between 3% to 50% oxygen by weight and average twice as many hydroxide groups as epoxide groups.[49–51] Our flake has 24 hydroxyl groups and 12 epoxide groups distributed in it with an additional 2 carboxyl groups at the outer edge of the flake. The is one realistic representation of graphene oxide flakes however many variations are possible based on synthesis conditions. It is our primary goal to characterize the effect of pore size. Thus, we will focus on this flake with the knowledge that oxidation level will require further studies.

Initial systems of PFAS and flakes were generated with Packmol[52] and minimized by steepest descent and conjugated gradient minimization prior to simulation. Dynamics were carried out using the leap-frog algorithm[53] to integrate the equations of motion, a cut-off distance of 8 Å for direct pairwise interactions, and particle mesh ewald[54] for the long-range electrostatics. A timestep of 1 fs was used and systems were equilibrated in an isobaric ensemble before moving to the isochoric ensemble for production runs. Analyses were performed using the cpptraj[55] MD analysis software as well as custom scripts. Graphics were rendered using Visual Molecular Dynamics (VMD).[56]

The pore transport simulations utilized harmonic restraints in Amber20 to keep three GO flakes merged to form triangular pores with specific diameters as defined by the largest sphere

that would fit within the vdW radii of the flake atoms. This geometry was chosen based on previous work with graphene oxide flakes, which in unbiased MD, exhibited stacking and agglomeration trends with shelf and triangular pocket formation.[36] Graphene oxide flakes and fully fluorinated graphene flakes were used to create separate pore systems to provide comparison between different types of hydrophobic pores. Pore diameters were set distances ranging from 6 Å to 16 Å. Fig. 1 depicts the different pores and graphene flakes used along with PFAS inside of them. The steered MD methodology was employed to thread PFAS through the pore, using the Jarzinsky relationship[57] to integrate the amount of work required to move from one end to the other end along a 30 Å path-length over the course of 5 ns for each pass. The length of time to get through the pore, *i.e.* the transport speed, impacts the amount of work required with slower speeds requiring less total work. The trends with respect to PFAS and pore size were seen to be

retained the same at 10 ns durations as well as at 5 ns (SI Fig. 1). Given the computational cost of the simulations, we decided to focus on calculating replicates with 5 ns pulls to ensure the trends are agnostic to the initial packing. The anionic form of the PFAS was used to represent the molecule as it is deprotonated at all environmentally relevant pH's. The bias force to pull the PFAS through the pore was calculated based on the position of the center of mass of the molecule relative to the ends of the pore, and forces acted equally on every atom in the PFAS. The molecule was moved both head-group-first, and tail-group-first through the pore and the two measurements were averaged together. No significant difference was observed between the two directions of motion indicating that the rate of motion was sufficiently slow to sample all pertinent configurations throughout the path. Three replicate simulations were performed for every data point. The data shown represents the average of the three replicates with error bars representing the standard deviation of the three.

Results

The adsorption process is driven by a combination of access and interaction strength of the solutes with the binding sites. The interaction strength, or thermodynamics, of the PFAS-flake binding are evaluated here using the linear interaction energy (LIE) formulism that sums up the van de Waals and electrostatic interactions between non-bonded molecules across the ensemble average of the molecular dynamics trajectory. As such, the absolute values of the LIE are very size-dependent and lack the effects of excluded volume within the solvent. Hence, discussion of the LIE results is only for relative comparison of the strength and type of interaction between different states in the same system.

Fig. 2 highlights the LIE results for each PFAS tested with each functionalized graphene flake as a function of pore diameter. Naturally, as the pore volumes increase the amount of interaction with the PFAS shifts more towards PFAS-water interactions and further away from PFAS-flake interactions. This stems from the contact surface area available to the molecule as the pore expands. More interestingly is the nonlinearity of that trend with a slight transition point in the slope of the PFAS-flake LIE visible around 11 Å in all systems. This critical diameter relates to the point at which PFAS within the pore can no longer interact with opposing flakes of the pore wall at the same time. Diameters above 11 Å result in inconsistent or competitive PFAS motions oscillating between one or two pore walls at a time but not all three. SI Fig. 2 shows that the structural variations as determined by root mean square displacements of the aligned trajectories do not depend on the pore size for all 4 flake types.

Looking further at Fig. 2, one can notice that the oxide (GOX) functionalized pores have nearly equivalent strength of binding interaction with all PFAS around −150 to −120 kcal mol^{-1} with decreasing interaction intensity as the pore size increases. The fully fluorinated pore walls (FFG) show trends opposite to the GOX with interaction strength getting more intense as pore diameter increases from 11 Å to 16 Å. This trend is driven by the
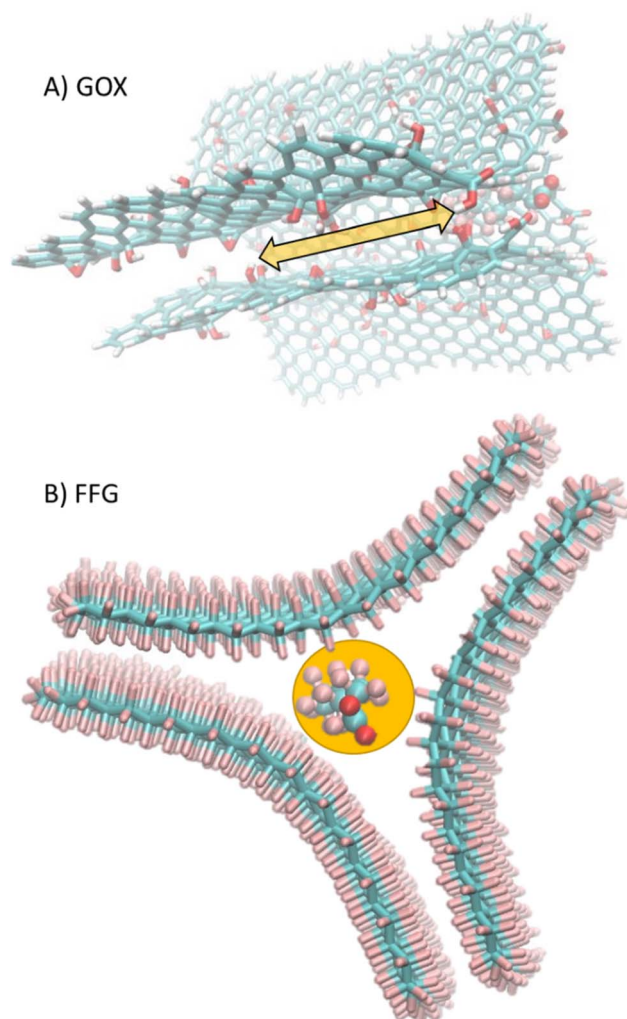

Fig. 1 Visual depiction of the functionalized flakes in triples to form extended contiguous pores of tunable size. (A) Graphene oxide flakes with arrow showing the inter-pore motion of the PFAS, (B) fully fluorinated graphene flakes with cylinder representing the pore volume and diameters used in analyses.

© 2025 The Author(s). Published by the Royal Society of Chemistry

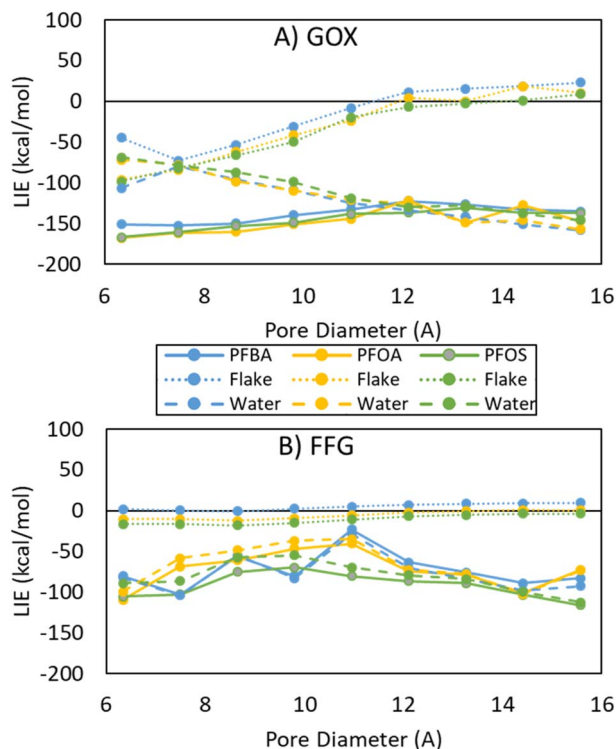*Environ. Sci.: Adv.*, 2025, **4**, 1587–1593 | **1589**

Fig. 2 Linear Interaction Energy (LIE) plots for PFBA (blue), PFOA (yellow), and PFOS (green) with the functionalized graphene flakes at various pore diameters. The linear interaction energy of each PFAS is broken down into the PFAS-flake interactions (dotted), PFAS-water interactions (dashed), and the total sum of the two (solid) for pore functionlizations of (A) graphene oxide flakes, and (B) fully fluorinated graphene flakes. Error bars make the plot unreadable, however variation between replicates is about 12% of the value on average. See SI Table 1 for more detail.

PFAS-flake component of the interactions which are much less favorable in FFG relative to GOX. While the fluorinated flakes create strong hydrophobic pockets, they do not create much interaction with the PFAS. The excluded volume of water–water interactions that push hydrophobic entities together are not well-captured by LIE analyses. SI Fig. 3 and 4 addresses this shortcoming of LIE through analyses of the contact statistics between PFAS and flake as well as between PFAS and water for all 4 flake types. The hydrophobic core of the FFG pore continue to exclude most PFAS-water contacts even at relatively large pore diameter up to 15 Å.

In addition to the thermodynamic trends of adsorption, using steered MD we can begin to probe kinetics of transport within porous modified graphene. As one might expect, chain length plays a significant role in the amount of work required to thread the PFAS through a pore. Fig. 3 highlights the results of steered MD threading PFAS through an idealized pore of modified graphene flakes made by anchoring three flakes together as shown in Fig. 1. Fig. 1(A) shows the work required to move the PFAS through as a function of the diameter of the pore within graphene oxide. Interestingly for all three PFASs there is minimum at a pore diameter of around 9 Å. At this diameter we see the PFAS are held in axial alignment with the pore axis and
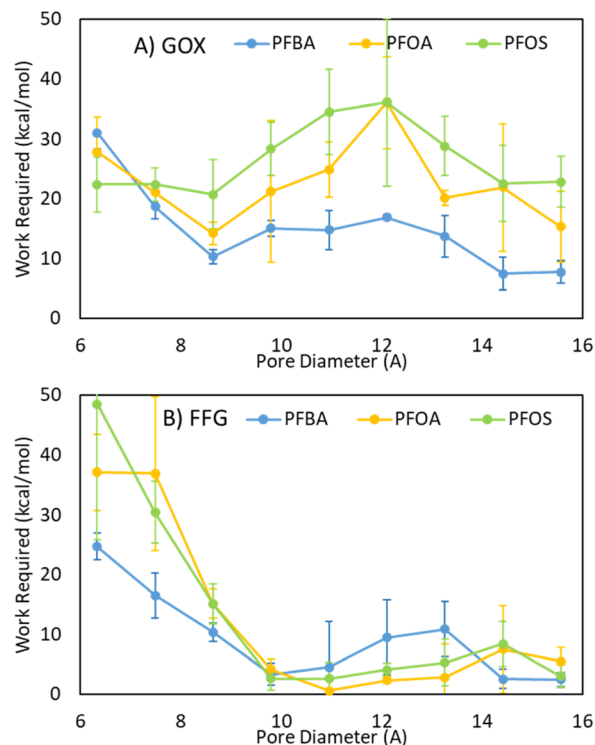

Fig. 3 PFAS mobility through graphitic pores, plotting the average work required to pull a PFAS molecule 20 Angstroms through the pore. (A) Graphene oxide flakes, (B) fully fluorinated graphene flakes.

transport through with relatively few sticking points to the oxidized graphene. At diameters of 8 Å or less the constriction of the pore walls greatly increases the resistance to transport through size-exclusion mechanisms. Around 13–14 Å there is a local maximum in the amount of work required for the transport of PFAS through the pore. In this pore size region, the PFAS is seen to kink and form multiple strong interactions with the pore walls at once. Beyond 15 Å the work required for transport tails off to a low value approaching the unconstrained level of diffusion across the surface. Similar trends exist for pores within fluorinated graphene shown in Fig. 3(B). Here we see that selectivity preferring sorption and transport of short chain PFAS is achieved in pores below 10 Å in diameter as evident from the lower work required to get through the pore. Conversely, in pores around 12 Å in diameter PFBA requires more work to transit the pore than PFOS or PFOA. Similarly, the work required to move PFAS through amide functionalized and partially fluorinated flakes, seen in SI Fig. 5, conserve the non-monotonic trends with respect to pore diameter. It is harder to get PFAS, especially longer chain PFAS, through a pore of 11 Å to 14 Å than it is to get PFAS through a pore of 9 Å. This non-linear trend of PFAS mobility with respect to pore size can be a design feature for PFAS-adsorbent materials. For example, a modified graphene material with pore sizes around 9–10 Å near the surface with larger internal pores in the 14–16 Å range can increase selectivity, binding efficacy and capacity for PFAS of the material as a whole. Alternatively, looking at selectivity between PFAS species, pore diameters of 12 Å or less will preferentially

allow shorter chain linear PFASs like PFBA to diffuse into the matrix more than longer chain PFASs like PFOA and PFOS. Depending on the desired application, these relationships between PFAS transport and pore size may help the selection of porous material for PFAS removal.

Conclusions

Classical molecular dynamic simulations of PFAS in porous structures of modified graphene show chain length dependence on optimum pore size that allows for selectivity. While short chain PFAS are more soluble, mobile, and harder to capture than longer chain PFAS, adsorbents with pore diameters around 10 Å are predicted to prefer PFBA over PFOA or PFOS. The sulfonate and carboxylate head groups of PFOS and PFOA respectively are seen to have minor impact on the amount of work required for pore transport with results being very similar between the two species. The thermodynamic driving force behind binding was seen to favor oxide functionalization over fluorination on the graphene flakes and the mechanism was driven by hydrophobic interactions from excluded solvent volume. Pore sizes of around 11 Å are critical turning point in the ratio of PFAS-flake interactions due to a decreased ability for the PFAS to interact on multiple sides at once. Functionalization of graphene oxide may create designable pore shapes and sizes as has been seen in alkylated flakes that resulted in preference for short chain PFAS adsorption.[36] Overall, these findings support the characterization and design of porous properties in enhanced adsorbent materials for PFAS capture and removal particularly when targeting short-chain PFAS species.

Author contributions

All authors contributed to the creation of this document. Dr Schutt conceived of the idea, executed the simulations, analyses and led the write-up of the results, conclusions, and abstract. Dr Bresnahan developed the modified graphene flakes to include structure and parameters of the materials and was primary writer on the introduction. Dr Ricard provided valuable insight to the research direction and execution of the simulations and edits to the manuscript. Dr Shukla provided high level guidance and direction on the focus, edits, and completion of the study and manuscript.

Conflicts of interest

There are no conflicts of interest to declare.

Data availability

The data supporting this article have been included in the main manuscript as well as part of the SI. SI data is attached to this submission in the form of a word document containing the results output by CPPTRAJ as the analysis package used to interpret AmberMD topology and trajectory files and plotted into charts. The trajectory files themselves are very large (100's of GB) and contain little intrinsic value outside of the extracted results already provided through analyses and graphs. Simulation inputs including forcefield parameters and molecular dynamics parameters are described in the methods section of the manuscript. See DOI: https://doi.org/10.1039/d5va00030k.

Acknowledgements

References

1 S. C. E. Leung, D. Wanninayake, D. Chen, N.-T. Nguyen and Q. Li, Physicochemical properties and interactions of perfluoroalkyl substances (PFAS) - Challenges and opportunities in sensing and remediation, *Sci. Total Environ.*, 2023, **905**, 166764.

2 J. Glüge, M. Scheringer, I. T. Cousins, J. C. DeWitt, G. Goldenman, D. Herzke, *et al.*, An overview of the uses of per- and polyfluoroalkyl substances (PFAS), *Environ. Sci.: Processes Impacts*, 2020, **22**(12), 2345–2373.

3 C. D. Vecitis, H. Park, J. Cheng, B. T. Mader and M. R. Hoffmann, Treatment technologies for aqueous perfluorooctanesulfonate (PFOS) and perfluorooctanoate (PFOA), *Front. Environ. Sci. Eng. China*, 2009, **3**(2), 129–151.

4 E. M. Sunderland, X. C. Hu, C. Dassuncao, A. K. Tokranov, C. C. Wagner and J. G. Allen, A review of the pathways of human exposure to poly- and perfluoroalkyl substances (PFASs) and present understanding of health effects, *J. Expo. Sci. Environ. Epidemiol.*, 2019, **29**(2), 131–147.

5 G. Jiménez-Skrzypek, J. González-Sálamo and J. Hernández-Borges, Analytical methodologies and occurrence of per- and polyfluorinated alkyl substances – A review, *J. Chromatogr. Open.*, 2023, **4**, 100089.

6 J. P. Giesy and K. Kannan, Global Distribution of Perfluorooctane Sulfonate in Wildlife, *Environ. Sci. Technol.*, 2001, **35**(7), 1339–1342.

7 C. A. Moody, G. N. Hebert, S. H. Strauss and J. A. Field, Occurrence and persistence of perfluorooctanesulfonate and other perfluorinated surfactants in groundwater at a fire-training area at Wurtsmith Air Force Base, Michigan, USA, *J. Environ. Monit.*, 2003, **5**(2), 341–345.

© 2025 The Author(s). Published by the Royal Society of Chemistry

Environ. Sci.: Adv., 2025, **4**, 1587–1593 | **1591**

8 K. Kannan, S. Corsolini, J. Falandysz, G. Fillmann, K. S. Kumar, B. G. Loganathan, *et al.*, Perfluorooctanesulfonate and Related Fluorochemicals in Human Blood from Several Countries, *Environ. Sci. Technol.*, 2004, **38**(17), 4489–4495.

9 M. Exner and H. Färber, Perfluorinated Surfactants in Surface and Drinking Waters (9 pp), *Environ. Sci. Pollut. Res.*, 2006, **13**(5), 299–307.

10 J. Hölzer, O. Midasch, K. Rauchfuss, M. Kraft, R. Reupert, J. Angerer, *et al.*, Biomonitoring of Perfluorinated Compounds in Children and Adults Exposed to Perfluorooctanoate-Contaminated Drinking Water, *Environ. Health Perspect.*, 2008, **116**(5), 651–657.

11 R. Monroy, K. Morrison, K. Teo, S. Atkinson, C. Kubwabo, B. Stewart, *et al.*, Serum levels of perfluoroalkyl compounds in human maternal and umbilical cord blood samples, *Environ. Res.*, 2008, **108**(1), 56–62.

12 Y. Pan, Y. Shi, J. Wang, Y. Cai and Y. Wu, Concentrations of perfluorinated compounds in human blood from twelve cities in China, *Environ. Toxicol. Chem.*, 2010, **29**(12), 2695–2701.

13 L. S. Haug, S. Huber, G. Becher and C. Thomsen, Characterisation of human exposure pathways to perfluorinated compounds — Comparing exposure estimates with biomarkers of exposure, *Environ. Int.*, 2011, **37**(4), 687–693.

14 B. M. Sharma, G. K. Bharat, S. Tayal, T. Larssen, J. Bečanová, P. Karásková, *et al.*, Perfluoroalkyl substances (PFAS) in river and ground/drinking water of the Ganges River basin: Emissions and implications for human exposure, *Environ. Pollut.*, 2016, **208**, 704–713.

15 A. Shankar, J. Xiao and A. Ducatman, Perfluoroalkyl Chemicals and Chronic Kidney Disease in US Adults, *Am. J. Epidemiol.*, 2011, **174**(8), 893–900.

16 M.-J. Lopez-Espinosa, D. Mondal, B. Armstrong, S. Bloom Michael and T. Fletcher, Thyroid Function and Perfluoroalkyl Acids in Children Living Near a Chemical Plant, *Environ. Health Perspect.*, 2012, **120**(7), 1036–1041.

17 V. Barry, A. Winquist and K. Steenland, Perfluorooctanoic Acid (PFOA) Exposures and Incident Cancers among Adults Living Near a Chemical Plant, *Environ. Health Perspect.*, 2013, **121**(11–12), 1313–1318.

18 C. R. Stein, K. J. McGovern, A. M. Pajak, P. J. Maglione and M. S. Wolff, Perfluoroalkyl and polyfluoroalkyl substances and indicators of immune function in children aged 12–19 y: National Health and Nutrition Examination Survey, *Pediatr. Res.*, 2016, **79**(2), 348–357.

19 D. M. Wanninayake, Comparison of currently available PFAS remediation technologies in water: A review, *J. Environ. Manage.*, 2021, **283**, 111977.

20 A. Kumar, W. A. Shaikh, H. M. Maqsood, S. J. Parikh and J. K. Biswas, Harnessing sustainable biochar-based composites for effective PFAS removal from wastewater, *Curr Opin Environ Sci Health*, 2025, **43**, 100594.

21 C. G. Bresnahan, T. C. Schutt and M. K. Shukla, Exploration of functionalizing graphene and the subsequent impact on PFAS adsorption capabilities via molecular dynamics, *Chemosphere*, 2023, **345**, 140462.

22 F. Mohd Jais, M. S. I. Ibrahim, A. El-Shafie, C. E. Choong, M. Kim, Y. Yoon, *et al.*, Updated review on current approaches and challenges for poly- and perfluoroalkyl substances removal using activated carbon-based adsorbents, *J. Water Proc. Eng.*, 2024, **64**, 105625.

23 P. S. Pauletto and T. J. Bandosz, Activated carbon versus metal-organic frameworks: A review of their PFAS adsorption performance, *J. Hazard. Mater.*, 2022, **425**, 127810.

24 F. Calore, E. Badetti, A. Bonetto, A. Pozzobon and A. Marcomini, Non-conventional sorption materials for the removal of legacy and emerging PFAS from water: A review, *Emerging Contam.*, 2024, **10**(3), 100303.

25 H. Li, A. L. Junker, J. Wen, L. Ahrens, M. Sillanpää, J. Tian, *et al.*, A recent overview of per- and polyfluoroalkyl substances (PFAS) removal by functional framework materials, *Chem. Eng. J.*, 2023, **452**, 139202.

26 M. E. Tighe, M. D. Thum, N. K. Weise and G. C. Daniels, PFAS removal from water using quaternary amine functionalized porous polymers, *Chem. Eng. J.*, 2024, **499**, 156280.

27 S. Thompson, A. M. Gutierrez, J. Bukowski and D. Bhattacharyya, Microfiltration Membrane Pore Functionalization with Primary and Quaternary Amines for PFAS Remediation: Capture, Regeneration, and Reuse, *Molecules*, 2024, **29**(17), 4229.

28 K. Liu, S. Zhang, X. Hu, K. Zhang, A. Roy and G. Yu, Understanding the Adsorption of PFOA on MIL-101(Cr)-Based Anionic-Exchange Metal–Organic Frameworks: Comparing DFT Calculations with Aqueous Sorption Experiments, *Environ. Sci. Technol.*, 2015, **49**(14), 8657–8665.

29 Y. Yang, Z. Zheng, W. Ji, J. Xu and X. Zhang, Insights to perfluorooctanoic acid adsorption micro-mechanism over Fe-based metal organic frameworks: Combining computational calculation with response surface methodology, *J. Hazard. Mater.*, 2020, **395**, 122686.

30 K. Sini, D. Bourgeois, M. Idouhar, M. Carboni and D. Meyer, Metal-organic frameworks cavity size effect on the extraction of organic pollutants, *Mater. Lett.*, 2019, **250**, 92–95.

31 W. Wang, Y. Jia, S. Zhou and S. Deng, Removal of typical PFAS from water by covalent organic frameworks with different pore sizes, *J. Hazard. Mater.*, 2023, **460**, 132522.

32 J. A. Sleep, S. J. Miklavcic and A. L. Juhasz, Modelling of PFAS-surface interactions: Effect of surface charge and solution ions, *Chemosphere*, 2023, **319**, 137910.

33 N. Loganathan and A. K. Wilson, Adsorption, Structure, and Dynamics of Short- and Long-Chain PFAS Molecules in Kaolinite: Molecular-Level Insights, *Environ. Sci. Technol.*, 2022, **56**(12), 8043–8052.

34 B. G. Lamb and B. Ma, PFAS self-assembly and adsorption dynamics on graphene: molecular insights into chemical and environmental influences, *Nanoscale*, 2025, **17**(17), 10632–10643.

35 D. Dey, T. Shafi, S. Chowdhury, B. K. Dubey and R. Sen, Progress and perspectives on carbon-based materials for

adsorptive removal and photocatalytic degradation of perfluoroalkyl and polyfluoroalkyl substances (PFAS), *Chemosphere*, 2024, **351**, 141164.

36 C. G. Bresnahan, T. C. Schutt and M. K. Shukla, A molecular dynamics investigation into manipulating graphene flake spacing for increased selectivity towards short chain PFAS capture, *Chemosphere*, 2025, **373**, 144135.

37 E. Mahofa, S. El Meragawi, M. A. Vilayatteri, S. Dwivedi, M. R. Panda, P. Jovanović, *et al.*, Manipulating Intrapore Energy Barriers in Graphene Oxide Nanochannels for Targeted Removal of Short-Chain PFAS, *ACS Nano*, 2025, **19**(15), 14742–14755.

38 C.-H. Huang, R. Lewis, S. Thomas, Z. Tang, J. Jones, S. Nason, *et al.*, Designing Ultraporous Mesostructured Silica Nanoparticles for the Remediation of Per- and Polyfluoroalkyl Substances, *ACS Nano*, 2025, **19**(21), 19777–19789.

39 B. Bezerra de Souza, J. A. Kewalramani, R. W. Marsh and J. Meegoda, Molecular Dynamics Simulation of the Impact of Functional Head Groups and Chain Lengths of PFAS Degradation Using Ultrasound Technology, *Water*, 2025, **17**(7), 1025.

40 B. D. Etz and M. K. Shukla, Per- and polyfluoroalkyl substances chemical degradation strategies: insights into the underlying reaction mechanisms, *Curr. Opin. Chem. Eng.*, 2023, **42**, 100956.

41 A. Gutiérrez, A. Maletta, S. Aparicio and M. Atilhan, A theoretical study of low concentration per- and polyfluoroalkyl substances (PFAS) remediation from wastewater by novel hydrophobic deep eutectic solvents (HDES) extraction agents, *J. Mol. Liq.*, 2023, **383**, 122101.

42 D. A. Case, K. Belfon, I. Y. Ben-Shalom, S. R. Brozell, D. S. Cerutti, T. E. Cheatham III, V. W. D. Cruzeiro, T. A. Darden, R. E. Duke, G. Giambasu, M. K. Gilson, H. Gohlke, A. W. Goetz, R. Harris, S. Izadi, S. A. Izmailov, K. Kasavajhala, A. Kovalenko, R. Krasny, T. Kurtzman, T. S. Lee, S. LeGrand, P. Li, C. Lin, J. Liu, T. Luchko, R. Luo, V. Man, K. M. Merz, Y. Miao, O. Mikhailovskii, G. Monard, H. Nguyen, A. Onufriev, F. Pan, S. Pantano, R. Qi, D. R. Roe, A. Roitberg, C. Sagui, S. Schott-Verdugo, J. Shen, C. L. Simmerling, N. R. Skrynnikov, J. Smith, J. Swails, R. C. Walker, J. Wang, L. Wilson, R. M. Wolf, X. Wu, Y. Xiong, Y. Xue, D. M. York and P. A. Kollman, *Amber 2020*, University of California, San Francisco, 2020.

43 K. G. Sprenger, V. W. Jaeger and J. Pfaendtner, The General AMBER Force Field (GAFF) Can Accurately Predict Thermodynamic and Transport Properties of Many Ionic Liquids, *J. Phys. Chem. B*, 2015, **119**(18), 5882–5895.

44 P. Bayly CIC, W. D. Cornell and P. A. Kollman, A Well-Behaved Electrostatic Potential Based Method Using Charge Restraints for Deriving Atomic Charges: The RESP Model, *J. Phys. Chem.*, 1993, **97**, 10269–10280.

45 J. Wang, W. Wang, P. A. Kollman and D. A. Case, Automatic atom type and bond type perception in molecular mechanical calculations, *J. Mol. Graph. Model.*, 2006, **25**(2), 247–260.

46 M. J. Frisch, G. W. Trucks, H. B. Schlegel, G. E. Scuseria, M. A. Robb, J. R. Cheeseman, *et al. Gaussian 16 Rev. C.02*. Wallingford, CT2016.

47 T. C. Schutt, G. A. Hegde, V. S. Bharadwaj, A. J. Johns and C. M. Maupin, Impact of Water-Dilution on the Solvation Properties of the Ionic Liquid 1-Methyltriethoxy-3-ethylimidazolium Acetate for Model Biomass Molecules, *J. Phys. Chem. B*, 2017, **121**(4), 843–853.

48 H. W. Horn, W. C. Swope, J. W. Pitera, J. D. Madura, T. J. Dick, G. L. Hura, *et al.*, Development of an improved four-site water model for biomolecular simulations: TIP4P-Ew, *J. Chem. Phys.*, 2004, **120**(20), 9665–9678.

49 C. K. Chua and M. Pumera, Chemical reduction of graphene oxide: a synthetic chemistry viewpoint, *Chem. Soc. Rev.*, 2014, **43**(1), 291–312.

50 W. Liu and G. Speranza, Tuning the Oxygen Content of Reduced Graphene Oxide and Effects on Its Properties, *ACS Omega*, 2021, **6**(9), 6195–6205.

51 F. Mouhat, F.-X. Coudert and M.-L. Bocquet, Structure and chemistry of graphene oxide in liquid water from first principles, *Nat. Commun.*, 2020, **11**(1), 1566.

52 L. Martínez, R. Andrade, E. G. Birgin and J. M. Martínez, PACKMOL: A package for building initial configurations for molecular dynamics simulations, *J. Comput. Chem.*, 2009, **30**(13), 2157–2164.

53 W. F. Van Gunsteren and H. J. C. Berendsen, A Leap-frog Algorithm for Stochastic Dynamics, *Mol. Simul.*, 1988, **1**(3), 173–185.

54 T. Darden, D. York and L. Pedersen, Particle mesh Ewald: An N·log(N) method for Ewald sums in large systems, *J. Chem. Phys.*, 1993, **98**(12), 10089–10092.

55 D. R. Roe and T. E. Cheatham, PTRAJ and CPPTRAJ: Software for Processing and Analysis of Molecular Dynamics Trajectory Data, *J. Chem. Theory Comput.*, 2013, **9**(7), 3084–3095.

56 W. Humphrey, A. Dalke and K. Schulten, VMD: Visual molecular dynamics, *J. Mol. Graph.*, 1996, **14**(1), 33–38.

57 C. Jarzynski, Nonequilibrium Equality for Free Energy Differences, *Phys. Rev. Lett.*, 1997, **78**(14), 2690–2693.

© 2025 The Author(s). Published by the Royal Society of Chemistry

Environ. Sci.: Adv., 2025, **4**, 1587–1593 | **1593**